ISTITUTO NAZIONALE DI RICERCA METROLOGICA
Repository Istituzionale

Integration of germanium-vacancy single photon emitters arrays in diamond nanopillars

Original
Integration of germanium-vacancy single photon emitters arrays in diamond nanopillars / Redolfi, Elisa; Pugliese, Vanna; Scattolo, Elia; Cian, Alessandro; Missale, Elena; Favaro De Oliveira, Felipe; Seniutinas, Gediminas; Ditalia Tchernij, Sviatoslav; Dell'Anna, Rossana; Traina, Paolo; Olivero, Paolo; Giubertoni, Damiano; Forneris, Jacopo. - In: EPJ QUANTUM TECHNOLOGY. - ISSN 2662-4400. - 12:1(2025). [10.1140/epjqt/s40507-025-00329-2]

Availability:
This version is available at: 11696/88465 since: 2026-02-27T15:38:32Z

Publisher:
Springer Science and Business Media Deutschland GmbH

Published
DOI:10.1140/epjqt/s40507-025-00329-2

Terms of use:

This article is made available under terms and conditions as specified in the corresponding bibliographic description in the repository

Publisher copyright

(Article begins on next page)

25 April 2026

Redolfi et al. *EPJ Quantum Technology* (2025) 12:25
https://doi.org/10.1140/epjqt/s40507-025-00329-2

EPJ Quantum Technology
a SpringerOpen Journal

RESEARCH Open Access

Integration of germanium-vacancy single photon emitters arrays in diamond nanopillars

Elisa Redolfi[1,2*], Vanna Pugliese[1], Elia Scattolo[3], Alessandro Cian[3], Elena Missale[3], Felipe Favaro de Oliveira[4], Gediminas Seniutinas[4], Sviatoslav Ditalia Tchernij[1,2], Rossana Dell'Anna[3], Paolo Traina[2], Paolo Olivero[1,2], Damiano Giubertoni[3] and Jacopo Forneris[1,2]

*Correspondence:
elisa.redolfi@unito.it
[1]University of Torino and Istituto Nazionale di Fisica Nucleare, sezione di Torino, 10125 Torino, Italy
[2]Istituto Nazionale di Ricerca Metrologica (INRiM), 10135 Torino, Italy
Full list of author information is available at the end of the article

Abstract

The nanoscale fabrication of μm-spaced single-photon emitter arrays is crucial for the development of integrated photonic chips. We report on the fabrication and systematic characterization of germanium-vacancy (GeV) color centers arrays in diamond obtained upon ion implantation at the nanoscale. Ge^{2+} ion implantations at 35 keV and 70 keV energies were carried out using a focused ion beam (FIB) equipped with a liquid metal alloy ion source. The arrays of emitters are subsequently aligned to ⌀300 nm nanopillar waveguiding structures, fabricated using a combination of electron-beam lithography and plasma etching. The photon collection efficiency and photoluminescence (PL) signal-to-background ratio increased by a factor 8 with respect to the unstructured sample. The photophysical properties of the GeV emitters fabricated by this approach were unaltered with respect to those found in unprocessed diamond. The efficiency of the overall manufacturing process to fabricate individual GeV centers was assessed. Up to 33% of the fabricated nanopillars, depending on ion implantation parameters, were found to contain single emitters.

Keywords: Single-photon sources; Diamond; Ion irradiation; Ion implantation; Formation yield; Nanowire; Collection efficiency; Photoluminescence; Nanopatterning

1 Introduction

The use of color centers in diamond emerged as a promising avenue for a variety of advanced applications in quantum technologies, ranging from high-precision sensing and quantum computing to secure communications [1, 2]. Among these, nitrogen-vacancy (NV) centers have attracted significant attention due to their specific opto-physical and spin properties, which allow for reliable operation under both ambient and cryogenic conditions [3]. However, in applications where spectral stability plays a key role such as quantum network nodes [2], NV centers have encountered challenges stemming from spectral instabilities determined by their strong sensitivity to local crystal environment [4]. In this context, alternative emitters based on group-IV color centers in diamond, such as silicon-vacancy (SiV) and germanium-vacancy (GeV) centers, demonstrated superior

© The Author(s) 2025. **Open Access** This article is licensed under a Creative Commons Attribution 4.0 International License, which permits use, sharing, adaptation, distribution and reproduction in any medium or format, as long as you give appropriate credit to the original author(s) and the source, provide a link to the Creative Commons licence, and indicate if changes were made. The images or other third party material in this article are included in the article's Creative Commons licence, unless indicated otherwise in a credit line to the material. If material is not included in the article's Creative Commons licence and your intended use is not permitted by statutory regulation or exceeds the permitted use, you will need to obtain permission directly from the copyright holder. To view a copy of this licence, visit http://creativecommons.org/licenses/by/4.0/.

spectral stability, and are considered better candidates in the aforementioned application areas [5–7].

These defects must be fabricated at the single-emitter level at a well-defined position in order to be easily embedded in light waveguides and coupling systems, enabling their integration in advanced quantum communication platforms together with a substantial enhancement in photon collection [8]. Ideally, manufacturing these waveguides should involve using pre-characterized and precisely localized arrays of color centers, rather than relying on the traditional top-down approach based on *a posteriori* selection of randomly placed color centers embedded in a homogeneous layer. The deterministic placement of individual single photon sources with high accuracy would result in a drastic advancement in quantum technology since this is a key requirement for the realization with good approximation of sources of states of light which, under synchronized pulsed excitation, would produce an exactly defined number of photons (i.e. with zero uncertainty), the so-called Fock states [9]. These states, eigenstates of the quantum photon number operator, are highly non-classical states and they are expected to be a fundamental tool in quantum metrology [10, 11] and sensing [12]. Furthermore, Fock states can be used for implementing boson sampling [13] and for the generation of other more exotic states of light such as Schrödinger cat states [14]. In addition to specific (and not addressed in this work) technical solutions enabling to optically excite a high-density array of emitters, a specific and reliable fabrication process is required: the most mature tool for this scope is ion implantation, which already represents a well-established and scalable process for solid state device fabrication in semiconductor technology [15]. Ion implantation allows the definition of the depth of the defects by tuning the ion implantation energy whereas the number of defects introduced in the material can be controlled by varying the ion fluence. However, applications based on individual quantum emitters require an extreme control of both defect location (<100 nm in all spatial dimensions) and number of implanted ions (ideally, $<10^2$ ions to create a single defect on the basis of typical formation yield values [16, 17]). Several approaches were reported in literature, including ion implantation through collimation nanoapertures [18] or patterned resist masks [19]. Among them, focused ion beam (FIB) technology offers several advantages: i) the relatively low ion energy (<100 keV) minimizes straggling and collision cascades, thereby reducing defect position uncertainty [20]; ii) ion beams can be focused to spot sizes down to 10 nm, i.e. comparable or smaller than the expected ion straggling; iii) sources enabling ∼pA ion beam current and pattern generator with 10-100 ns beam dwell time allow implanting at fluences down to the single ion level [21]. Finally, being the FIB a direct writing process, defects can be created at desired positions in a mask-less process with excellent overlay with the support of a highly accurate sample positioning system (e.g. a laser interferometric stage) [22]. To date, NV [23], SiV^- [24, 25] and GeV^- [25, 26] single photon emitters fabricated in diamonds by FIB have been reported in literature, as well as V_{Si} in SiC [22] or G and W centers in Si [27].

Still, manufacturing protocols of these color centers are currently under exploration due to limitations in formation yield (few percents for split-vacancy-type defects in diamond) and reproducibility [6, 17], which are crucial requirements for their embedment in nanostructures such as photonic waveguides [7].

Furthermore, the delivery of small ion fluences to nm-sized target volumes in the host material could result in the introduction of significant local structural damage which could hinder the emission properties of the fabricated emitters. This drawback might be critical when the aforementioned modest formation yield requires the introduction of tens of ions to nm spot sizes, in order to ensure the formation of individual emitters.

In this paper, we explore the effects of the localized formation of GeV centers [28] upon germanium implantation via FIB technology, reporting for the first time their large-scale fabrication and embedment in nanopillars. This approach allows for a comparison of the emission properties before and after the nanopillar fabrication and significantly reduces, in perspective, the experimental effort to find suitable color centers. By combining the fabrication of arrays of color centers with the nanopillar fabrication process, offering a ∼8-fold enhancement in the photon collection with respect to unstructured samples, we facilitate the characterization of points of interest, with an emphasis on the single-emitters occurrence, their emission properties and the effects of radiation-induced lattice damage.

2 Methods

2.1 Sample fabrication

The schematic overview of the fabrication process is shown in *Fig. 1*. The whole process is described in detail in the following.

2.2 Material

The present work was performed on a commercially available single-crystal [100]-oriented electronic-grade bulk diamond sample [29]. Before the fabrication of color centers and nanofabrication, the sample was cut and polished into a thin (4x4x0.05) mm^3 membrane with a resulting surface roughness below 1 nm. Particular care was taken to perform the polishing process without inducing significant sub-surface damage to the diamond lattice [30].

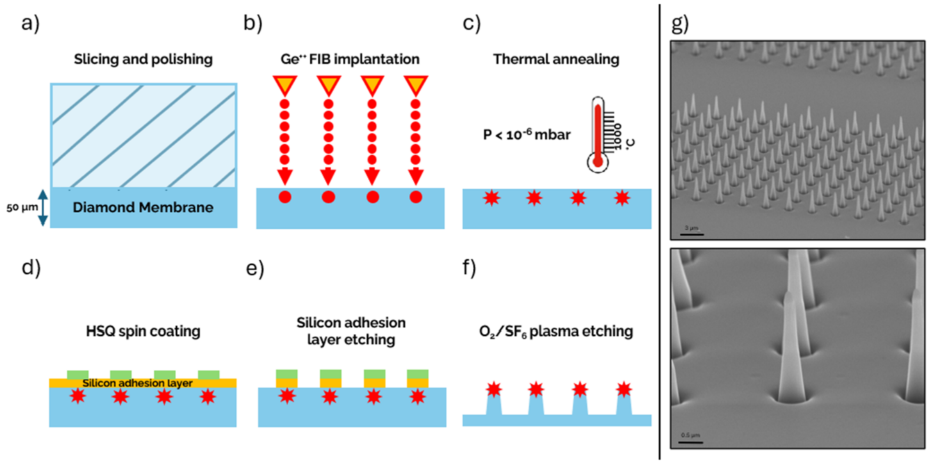

Figure 1 Schematic overview of the fabrication process and SEM images during and after the manufacturing of nanopillar arrays. *(a)* Cut and lapping of bulk diamond to obtain a 50 μm thick diamond membrane. *(b)* 35 and 70 keV Ge^{++} implantation by FIB (SRIM expected projected ranges: 17.5 and 29.8 nm, respectively). Ion implantation details are reported in Sect. 2.3, while the implantation profiles are described in Sect. 2 and Fig. 4. *(c)* Thermal annealing at 1000 °C temperature and $<10^{-6}$ mbar pressure. *(d)* Silicon adhesion layer deposition and e-beam patterning of HSQ resist. *(e)* Silicon adhesion layer etching by plasma. *(f)* Nanopillars pattern transfer to the diamond membrane by plasma etching. *(g)* SEM image (top) acquired at a 15° angle from the array of etched pillars, and SEM image (bottom) of a single pillar showing the truncated cone shape and resulting etched surface quality

Table 1 Experimental parameters adopted for the FIB implantation of Ge^{++} ions. Ions fluences expressed as cm^{-2} are calculated from the spot dose and spot size, assuming a circular beam of diameter corresponding to the spot size

Acceleration (kV)	Energy (keV)	Beam current (pA)	Beam spot size (nm)	Spot dose (ions/spot)	φ ion fluence (x10^{12} ions/cm^{-2})
35	70	3.15	25 ± 5	40; 60; 80; 120; 160; 800	8.2; 12; 16; 24; 33; 160
17.5	35	1.88	25 ± 5	35; 52; 70; 105; 140; 700	7.1; 11; 14; 21; 28; 140

2.3 Ion implantation

Ge^{++} ion implantation was carried out locally using a focused ion beam - scanning electron microscope (FIB-SEM) equipped with a liquid metal alloy ion source (Au-Ge-Si composition) and a laser interferometric stage (Raith Velion). The patterning was carried out in two phases: in the first, an intense 35 keV Au^{+} beam was used to pattern deep alignment markers (~ 1 μm) for both FIB Ge irradiation and nanopillars electron beam lithography (EBL). Such markers were designed to allow for a sub-100 nm overlay accuracy between the implantation arrays and subsequent fabrication of nanopillars. In the second step, Ge^{++} implantation was carried out with acceleration voltages of either 35 or 17.5 kV resulting in kinetic energies of either 70 keV or 35 keV, respectively. Small apertures in the FIB column defined the beam spot size (25 ± 5) nm and current ($\sim$1pA). Ge^{++} irradiations were performed upon alignment with the previously defined Au^{+} markers. Square arrays of 40x10 spots (3 μm spacing) were implanted for each implantation energy and investigated spot dose in the $\sim$30–800 ions/spot range (see *Table 1*).

The ions/spot dose values can be converted into ions/cm^2 fluence values φ, defined according to the Poisson distribution using the ion current I_{ion} measured by a Faraday cup (corrected for background current) and the dwell time settings t_{dwell} of the pattern generator (minimum value: 20 ns). We considered a circular implanted surface having a diameter d equal to the above-mentioned beam spot size.

$$\varphi = \frac{I_{ion} \cdot t_{dwell}}{\pi \cdot \left(\frac{d}{2}\right)^2} \tag{1}$$

Following ion implantation, the sample was thermally treated in high vacuum ($p < 10^{-6}$ mbar) for two hours at a preset temperature of 1000 °C to promote the formation of stable, optically-active GeV centers [31].

2.4 Nanopillars fabrication

After the manufacturing and initial characterization of the color center arrays, nanopillars were fabricated using a combination of EBL and plasma etching, by following similar procedures as described in [32].

A 20 nm thick silicon adhesion layer was electron-beam-evaporated on the sample surface, thus enabling the subsequent spin-coating of hydrogen silsesquioxane (HSQ). The same fiducial markers were used to align the creation of the HSQ mask for the nanopillars with the existing array of color centers (*Fig. 1d*). This alignment was automatically performed using the overlay functionality of the EBL setup (Vistec EBPG 5000PlusES), achieving a spatial accuracy which was estimated within 40 nm. After exposure of the HSQ mask, the silicon adhesion layer was removed using SF_6 plasma (*Fig. 1e)*. The fabrication process resulted in stacks of HSQ/silicon that would act as the etching mask defining the bright (i.e. color-center embedding) locations. Plasma etching of the nanopillars employed intermixed steps of pure O_2 and a combination of O_2 and SF_6 to create tapered nanopillars while preventing the formation of micro-masking at the etched surface (*Fig. 1f)*. The sample was etched to a depth of approximately 2.2 μm, resulting in nanopillars with a truncated cone geometry, featuring a top surface diameter of 300 nm—where the GeV centers are located—and a bottom aperture of approximately 650 nm (*Fig. 1g*). Such waveguides are known to be multi-modal: this feature has been proven to enhance the collection efficiency of the emitted light [33]. After etching the nanopillars, the remaining HSQ mask was removed in 10% hydrofluoric (HF) acid. The sample was then thoroughly rinsed with DI water and immersed in 20% potassium hydroxide (KOH) solution to remove the remaining silicon layer. Finally, the sample was again rinsed with DI water and cleaned using a tri-acid boiling treatment [34] to remove any graphitic layers and to oxidise the surface.

2.5 Photoluminescence characterization

The sample was systematically characterized with photoluminescence (PL) technique. The PL characterization was carried out using a custom fiber-coupled single-photon sensitive confocal microscope (100x objective, 0.9 NA (Numerical Aperture)), where the excitation was provided by a 505 nm CW (Continuous Wave) laser with 5.52 mW excitation power, and the collection was performed by coupling the system to a 0.22 NA multimode optical fiber feeding a pair of commercial silicon-based single-photon avalanche diodes (Si-SPADs) with ∼100 cps dark count rate and ∼45 ns deadtime operating in free-running mode. The typical photon detection efficiency of the above-mentioned detectors is ∼50 % at 520 nm wavelength. The utilization of a dichroic mirror and a longpass filter ensured the characterization of emission wavelengths greater than 550 nm, thus filtering out the first-order Raman emission (541.4 nm for the considered excitation wavelength). An additional (600 ± 10) nm bandpass filter was inserted in the collection path for the sole characterization of GeV single-photon emitters, due to their preponderant emission at 602 nm. The confocal microscope was equipped with a Hanbury-Brown and Twiss (HBT) interferometer, based on a collection fiber connected to two SPADs employing a fiber-fused 50:50 beamsplitter [35]. The spectral characterization was performed by means of a PIXIS camera coupled with a SpectraPro HRS 300 spectrometer with a resolution of 0.2 nm and a spectral operation range of 330-800 nm.

3 Results and discussion

Fig. 2a-b show the confocal PL maps, acquired using a 550 longpass optical filter, from the regions implanted at 70 keV energy (800 ions/spot) before and after the nanopillars manufacturing. The maps show a set of diffraction-limited luminescent spots arranged along the regular geometry and spacing defined by the above-described fabrication process.

Although the same optical excitation power (5.52 mW) was applied, the PL intensity scales differ due to the different topography around the GeV centers. Notably, the fluorescence behaviour of color center arrays prior to nanostructuring (∼0.3 Mcps including background emission) is significantly less intense than that acquired from nanopillar structures (up to 2 Mcps). In addition to the overall emission intensity increase, *Fig. 2* also highlights the dramatic enhancement in signal-to-background ratio achieved after nanopillar fabrication (up to a factor 8) with respect to the unstructured surface (i.e. a ∼2 increase factor for the array implanted with 800 ions/spot). Indeed, the background emission in *Fig. 2a* corresponds both to the sample surface reflection of the excitation laser

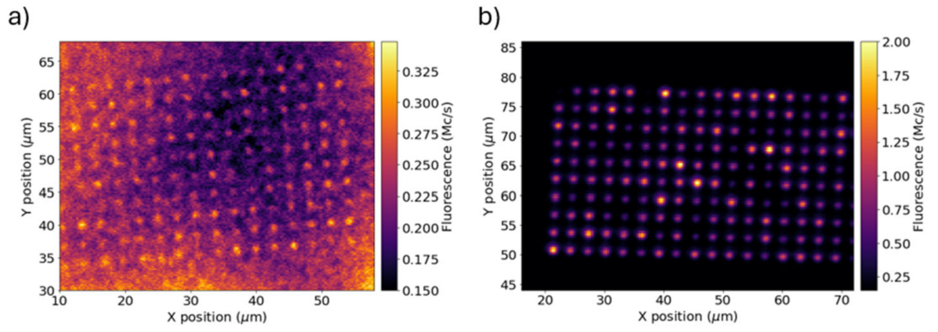

Figure 2 Confocal images acquired using a 550 nm longpass optical filter with 5.52 mW excitation power before *(a)* and after *(b)* nanopillars fabrication for the 800 ions/spot region at 70 keV implantation energy. In (b) the PL intensity and the signal-to-background ratio are improved by the nanopillars with respect to the unstructured surface (a). Images in (b) are acquired by imaging the nanopillars through their back aperture in order to leverage the photonic waveguiding properties of such structures

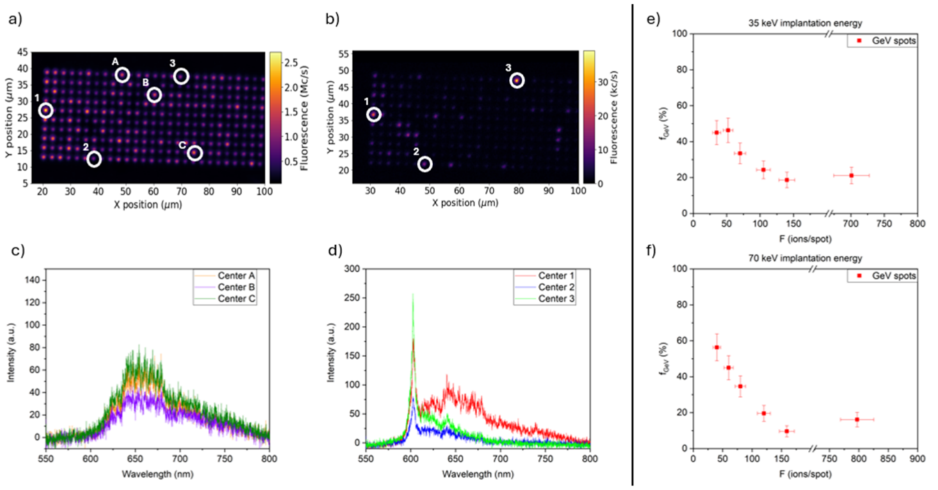

Figure 3 *(a-b)* PL images of a region implanted with 70 keV energy and 120 ions/spot, under 5.52 mW excitation power. (a) PL scan acquired with 550 nm longpass optical filter. (b) PL scan acquired with a (600 ± 10) nm bandpass filter. *(c-d)* PL spectra of the emitting nanopillars highlighted in (a) and (b) acquired with 0.25 mW excitation laser power. (c) Spectra of spots visible only in the not-filtered scan image and (d) of spots visible in both scan images. *(e-f)* Number (f_{GeV}) of GeV-containing pillars (in %) as a function of the ions/spot doses (F) for 35 keV (e) and 70 keV (f) implantation energies. The error bars summarize the Poisson uncertainty

and the NV PL emission (described in the following paragraph) since the excitation laser is maximally focused within the confocal volume under investigation. On the other hand, in *Fig. 2b* the signal is collected only from the top of the nanopillars which is located 2.2 μm above the contributing background.

To offer further insight into the outcome of the fabrication process, we turn our attention to the confocal PL scan obtained from the nanopatterned sample using the 550 nm longpass filtering, as shown in *Fig. 3a*. The map was acquired from the sample region fabricated with 70 keV Ge implantation and 120 ions/spot dose.

Subsequently, the same region was PL-mapped with a (600 ± 10) nm bandpass filter to select the sole emission originating from GeV centers, and the corresponding results are shown in *Fig. 3b*. The two maps show a significant difference in the recorded PL intensities:

the overall photon count rate detected at wavelengths >550 nm (*Fig. 3a*) amounts to ∼2.5 Mcps for each spot, while it decreases down to ∼35 kcps when the filtering restricts the collection to the GeV ZPL (*Fig. 3b*). In addition, *Fig. 3a* exhibits a bright PL emission from the vast majority of the spots of the array, while *Fig. 3b* shows that the emission of GeV is collected from a limited number of nanopillars.

To investigate the nature of the emitting spots, a set of nanopillars (circled in white in *Fig. 3a-b*) was selected for a more extensive PL characterization. Firstly, a spectral characterization (0.25 mW excitation power) was performed in the 550 – 800 nm spectral range. *Fig. 3c* shows the spectra acquired from the spots highlighted with letter (A, B, C) labels in *Fig. 3a*, which do not correspond to any detectable PL signal under (600 ± 10) nm bandpass filtering (*Fig. 3b*). The vast majority of their PL emission is located in the 640-680 nm spectral range, which is compatible with attribution to the negative charge state of NV centers. Conversely, the spectra acquired from the spots highlighted with number (1, 2, 3) labels (which appear as luminescent in both *Fig. 3a-b*) reveal the occurrence of the ZPL of the GeV center (*Fig. 3d*) [36]. This emission is in some instances accompanied by a broader emission at higher wavelengths, denoted by a ZPL peak at ∼640 nm, which is attributed to non-filtered emissions of NV centers within the same nanopillar [37]. The observed concurrent formation of NV centers in the fabrication process cannot be interpreted as a by-product of Ge implantation, i.e. the introduction of lattice vacancies in a diamond substrate, since the ∼5 ppb content of native nitrogen (∼$9\text{x}10^{-7}$ atoms nm^{-3}) is insufficient to promote the formation of a sufficient amount of centers. Conversely, the number of substitutional N atoms included in the nanopillar volume (calculated considering a constant radius of 150 nm and 2.2 μm height) is ∼115 atoms. Assuming a 15% occurrence of NV centers with respect to the N content [38], ∼17.3 optically active NV centers (each one with PL intensity of 100-300 kcps [8]) can be expected. This amount is compatible with the PL count rate reported in *Fig. 3a*, suggesting that the strong PL signal originates from the waveguiding of the emission of natively occurring centers within the nanopillar volume. On the other hand, the introduction of N in the sample during the implantation process can be ruled out on the basis of the ion source specifications and the adopted experimental configuration based on a mass selection system. From a practical point of view, however, the coexistence of both NV and GeV centers does not represent a limiting factor for the utilization of either class of emitters, since they can be discriminated by spectral filtering.

An estimate of the efficiency of the manufacturing production to achieve single GeV center formation was firstly assessed on the basis of the ion fluence by analysing the PL maps acquired with the (600 ± 10) nm bandpass filter with 5.52 mW optical excitation power. In this case, the fraction of fabricated nanopillars which displayed GeV emission was quantified on the basis of the intensity distribution of the spot arrays. The presence of at least one GeV center in such nanopillars was assessed by setting a threshold in the PL intensity above 30 kcps. This threshold value was determined on the basis of the systematic characterization of the emission properties at the set optical power (see the following Section).

In *Fig. 3e-f* the relative occurrence of GeV centers (f_{GeV}) in the fabricated nanopillars (i.e. the fraction of nanopillars exhibiting emission from at least one GeV center) is reported as a function of the implanted spot dose (F). The maximum value is found for the lowest considered spot doses of 35-40 ions/spot. In this case, for both implantation energies a $f_{GeV} \sim 0.5$ occurrence was found. Such value is in agreement with the formation yield of individual GeV emitters (0.6-1.9%) upon ion implantation in similar experimental conditions [25, 26]. It is also worth noting that, for both 35 keV and 70 keV implantation energies (E), the number of pillars containing GeV emitters decreases at increasing ion fluences. This result could be related to misalignment of the fabrication processes, e.g. related to the progressive charge build-up in insulating diamond as a result of ion implantation. However, since the irradiation patterning was the same for the two tested implantation energies, one would expect the same effect for the two arrays or even a worse result for the lower energy (which is more affected by charging), while the results exhibit the opposite trend.

Further context can be provided by considering the implanted ion fluence, i.e. in the $2.1 \cdot 10^{13}$ - $1.6 \cdot 10^{14}$ cm^{-2} range (see *Table 1*) [39]. "Stopping and Range of Ions in Matter" (SRIM) simulations [40, 41] were performed to investigate the effects of radiation damage and/or lattice amorphization [42–44]. *Fig. 4a-b* show the concentration of displaced C atoms as a function of the implantation depth for each implantation fluence. The graphitization threshold (i.e. the vacancy density at which the heavily damaged diamond lattice converts to graphitic phase upon thermal annealing) is also shown, with a value of $\sim 6 \cdot 10^{21}$ cm^{-3} assumed on the basis of previous experimental works [44].

The formation of an amorphous or a graphitized layer becomes increasingly likely for the highest spot doses under both 35 keV (*Fig. 4a*) and 70 keV (*Fig. 4b*) implantation energies, explaining the decreasing trend in the GeV occurrence shown in *Fig. 3e-f*, also considering the etching and the subsequent tri-acid cleaning carried out during and after nanopillar formation, respectively. In addition to such mechanism, a high density of vacancies within

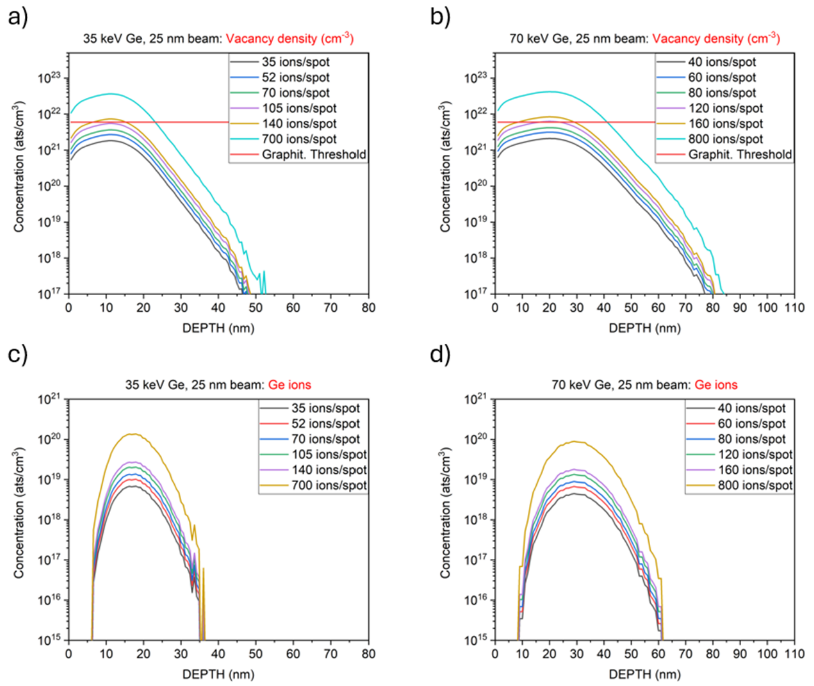

Figure 4 SRIM simulation of the displaced C atoms as a function of the depth for 35 keV *(a)* and 70 keV *(b)* implantation energies and SRIM simulations of the Ge ions concentration as a function of the depth for 35 keV *(c)* and 70 keV *(d)* implantation energies

the diamond lattice will also result in an increased probability of the formation of vacancy complexes such as di-vacancies [45], which will compete with the formation of color centers in the implanted diamond lattice.

For all the considered spot doses, the vacancy density exhibits the highest values ($>1 \cdot 10^{20}$ cm^{-3}, roughly corresponding to 100 ppm) within 20 nm (30 nm) for 35 keV (70 keV) implantation energy, and it is significantly lower at the tail of the Ge ion depth distribution (*Fig. 4c-d*), the latter extending to depths of 35 nm (60 nm). Therefore, the Ge ions implanted within the most damaged or amorphized layer might not result in the formation of GeV color centers due to extreme lattice damage, leaving the formation of optically active defects only at the layers beneath. Thus, it is likely that the formation yield decreases at increasing spot dose shown in *Fig. 3e-f* can be attributed to the thickening of the heavily damaged layer.

3.1 Single-photon emitters characterization

The successful incorporation of individual GeV centers by the aligned fabrication process was assessed by performing systematic HBT interferometry. For the sake of statistical significance, the second-order autocorrelation function $g^2(\tau)$ [46] was acquired from 15 randomly selected nanopillars displaying GeV emission for each implantation fluence and energy. The criterion to determine the presence of single-photon emitters was a value of the background-uncorrected function at zero delay time $g^2(\tau = 0)$ smaller than 0.5 [46]. In *Fig. 5a* a typical $g^2(\tau)$ function measurement corresponding to a single photon emitter (selected in the 105 ions/spot region at 35 keV energy) is shown [47, 48].

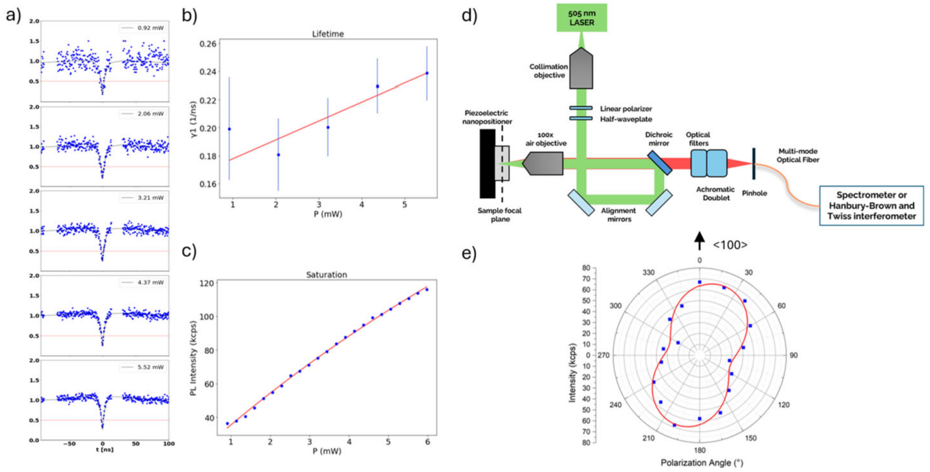

Figure 5 Single emitter effective lifetime and saturation characterization example (35 keV energy - 105 ions/spot region). *(a)* $g^2(\tau)$ data acquired at different excitation power using the (600 ± 10) nm bandpass filter to select only GeV-related emission. The missing points are related to the removal of the backflash peaks originated by the counter-propagation of photons in the fiber-coupled HBT interferometer. *(b)* Dependence of the γ_1 parameter obtained by each $g^2(\tau)$ fit on the excitation power. *(c)* Saturation curve. The PL intensity is the sum of the emitter count rates obtained by both detectors. The saturation plateau was not reachable since the maximum laser power adopted in the experiment was 6 mW. *(d)* Schematic representation of the confocal setup, where the excitation laser radiation and the PL emission are represented in green and in red, respectively. The setup is described in Sect. 2.3. *(e)* Emission intensity as a function of the excitation laser polarization. The red line is the sine-based function used to fit the data

The single-photon-level characterization of GeV centers also allows to estimate relevant emission parameters, namely the excited state lifetime, the emission intensity and optical power at saturation.

According to the three-level system model [49], the $g^2(\tau)$ curves acquired at different excitation powers (*Fig. 5a*) were fitted according to the function:

$$g^2(\tau) = 1 - (1 - a) \cdot exp(-|t| \cdot \gamma_1) + a \cdot exp(-|t| \cdot \gamma_2) \tag{2}$$

where a is a parameter that estimates the antibunching effect at $t = 0$ delay, t is the emission delay between two subsequent photons, and γ_1 and γ_2 are parameters related to the antibunching and bunching characteristic times.

Since the parameter γ_1 has a linear dependence on the excitation power P (*Fig. 5b*) [50], the results were fitted with the simplified function:

$$\gamma_1 = m \cdot P + 1/\tau \tag{3}$$

where τ is the effective lifetime, which was equal to $\tau = (6.08 \pm 0.09)\ ns$ for the exemplary emitter in *Fig. 5a*. This value is in line with the results reported in literature [36, 51, 52]. Similarly, the saturation curve is shown as an example in *Fig. 5c*, which displays the PL intensity $I(P)$ versus the optical excitation power P. The data were fitted according to the equation [49]:

$$I(P) = I_{sat} \cdot P/(P + P_{sat}) \tag{4}$$

where the emission intensity and excitation power at saturation are, for the considered emitter, $I_{sat} = (268 \pm 15)\ kcps$ and $P_{sat} = (7.6 \pm 0.6)\ mW$, respectively.

The emission polarization was measured by placing at the excitation laser output a fixed linear polarizer and a half-waveplate mounted on a motorized stage. A schematic representation of the experimental setup is shown in *Fig. 5d* (setup description in Sect. 2.3), where it is possible to identify the three optically conjugate points of the confocal microscope, namely: the excitation laser, the focal point on the sample and the pinhole. The polarization pattern (*Fig. 5e*) of the emitter under consideration was obtained by changing the polarization of the excitation laser (i.e. the angle of the half-waveplate) and collecting the emitted PL. The red line is the sine-based function used to fit the data points.

The data suggest a linear polarization, (in line with results obtained from nanodiamond-embedded emitters [53]) with a 41% visibility, and with the polarization axis aligned to the expected crystal bond angle of diamond. The non-negligible emission from the equatorial plan of the dipole is in line with the presence of an additional emission dipole, in reasonable agreement with what reported for other split-vacancy such as the SiV [54] and SnV [55] color centers.

The relative distribution of the effective lifetime, saturation power and intensity, and ZPL values obtained for the single emitters found are shown in *Fig. 6*. The results obtained from 35 keV and 70 keV implantation energies were aggregated since no significant statistical differences were observed.

The median value of each distribution is reported with the median absolute deviation in *Table 2*. All the values are in good agreement with values reported in the literature

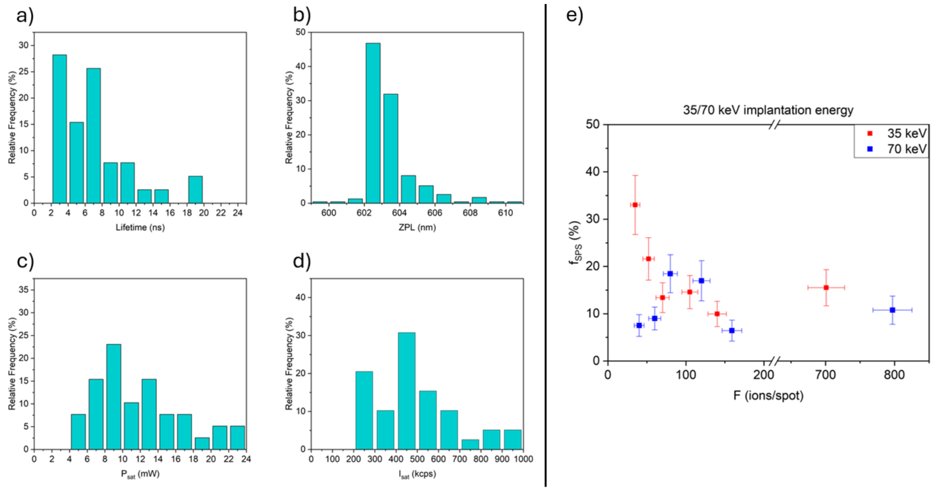

Figure 6 Effective lifetime *(a)*, ZPL *(b)*, saturation power *(c)* and saturation intensity *(d)* distribution of the whole dataset of single emitters characterized. *(e)* Relative occurrence of single emitters as a function of the ions/spot doses for 35 keV and 70 keV implantation energies. The error bars summarize the Poisson uncertainty

Table 2 Median values with associated median absolute deviations of effective lifetime, ZPL, saturation power and intensity

	Median value
Effective lifetime (ns)	6 ± 5
ZPL (nm)	603 ± 4
P_{sat} (mW)	12 ± 6
I_{sat} (kcps)	470 ± 240

[28, 36, 51, 52] indicating that the relevant emission parameters of the GeV centers remain largely unaffected by the high vacancy density generated by the nanoscale ion implantation process, as well as by the fabrication process of the nanopillars.

As a final step, the relative occurrence $f_{SPS}(E, F)$ of nanopillars incorporating one single GeV emitter was evaluated as the fraction $f_{exp}(E, F)$ of the 15 experimentally investigated spots at each implantation condition (i.e. ion energy (E) and implantation spot dose (F)), multiplied by the fraction $f_{GeV}(E, F)$ of the fabricated nanopillars displaying the spectral signature of GeV emission. This quantity describes the overall effectiveness of the entire fabrication process to deliver a single-photon emitter given the implantation of N_i ions on each individual implantation spot:

$$f_{SPS}(E,F) = f_{GeV}(E,F) \cdot f_{exp}(E,F) \tag{5}$$

The resulting occurrence of single emitters is shown in *Fig. 6e* for each implantation energy as a function of the ions/spot implantation dose.

For both implantation energies, the relative occurrence of single emitters is ranging from 6% to 33% denoting a satisfactory outcome of the whole fabrication process. It is worth stressing that the observed decrease in the $f_{SPS}(F)$ at higher doses is associated to the formation of an amorphous or a graphitized layer as discussed in the previous section. However, this trend was not apparent for doses below 80 ions/spot implanted at 70 keV (value for which the maximal effectiveness is found for the considered energy), where the higher vacancy density associated with each ion impact might favour the formation of multiple GeV centers at individual nanopillar sites also at the lower spot doses (i.e. the number of clusters is higher than the one of single photon emitters) as reported in [26, 56]. These data thus suggest a higher formation yield for 70 keV ion implantation, which is mitigated by the damage cumulation in the diamond lattice at increasing ion fluence.

4 Conclusions

In this work, a systematic study on the formation and single-photon emission properties of GeV diamond color centers arrays embedded in nanopillars by FIB irradiation and post-implantation aligned etching has been conducted. The nanopillars fabrication resulted in the embedment of single GeV centers with a resolution of 300 nm by construction and led to an enhancement up to a factor of 8 of the signal-to-background ratio with respect to the unstructured surface, allowing to selectively study GeV centers.

The overall GeV fluorescence, even at the ensemble emission level, exhibited a decreasing trend at increasing implantation fluences. This result might be indicative of the introduction of significant radiation-induced lattice disorder at increasing fluences, reaching the graphitization threshold at the highest considered values [44].

A systematic study of GeV centers at the single-photon emitter level at all the considered implantation fluences evidenced emission properties (excited state effective lifetime, optical power and emission intensity at saturation, ZPL central wavelength) in line with what reported in the literature [28, 36, 51, 52]. Finally, the considered fabrication process resulted in the occurrence of single-photon emitting GeV centers in up to 33% of the fabricated nanopillars for the optimal set of implantation parameters (35 keV implantation energy, 35 ions/spot dose).

These results indicate that the proposed approach to nanoscale fabrication, based on FIB ion implantation and subsequent coupling to waveguiding nanopillars, is viable for practical technological applications. In particular, the nanoscale fabrication of large arrays of high-density, diffraction limited, μm-spaced single-photon emitters could enable the development of integrated photonic chips for parallel quantum information processing [57, 58] and for the generation of Fock states with a large number of photons [59].

Abbreviations

CW, Continuous Wave; DI, Deionized; EBL, Electron Beam Lithography; FIB, Focused Ion Beam; GeV, Germanium-Vacancy; HBT, Hanbury-Brown and Twiss; HSQ, Hydrogen Silsesquioxane; NA, Numerical Aperture; NV, Nitrogen-Vacancy; PL, Photoluminescence; SEM, Scanning Electron Microscope; SiC, Silicon Carbide; SiV, Silicon-Vacancy; SnV, Tin-Vacancy; SPAD, Single-Photon Avalanche Diode; SRIM, Stopping and Range of Ions in Matter; ZPL, Zero Phonon Line.

Acknowledgements

Not applicable.

Author contributions

E.R., J.F., D.G. and F.F.O. designed the experiments and the characterization procedure. E.S., A.C., E.M., R.D.A. and D.G defined and performed the ion implantation process. F.F.O. and G.S. prepared the diamond membrane and performed the nanopillars fabrication. E.R., V.P. and P.O. developed the confocal microscopy system. E.R, V.P., P.T, and S.D.T. performed the thermal processing and the PL characterization. E.R. led the PL characterization and curated the data analysis. E.R. P.O. and J.F. prepared the original draft of the manuscript. All authors reviewed and edited the manuscript.

Funding

This work was supported by the following projects: Project “Piemonte Quantum Enabling Technologies” (PiQuET), funded by the Piemonte Region within the “Infra-P” scheme (POR-FESR 2014-2020 program of the European Union); the project GeVIon-Q funded by the Q@TN- “Quantum Science and Technology in Trento” consortium; experiments ROUGE, QUISS funded by the 5th National Commission of the Italian National Institute for Nuclear Physics (INFN). J.F. acknowledge financial support under the National Recovery and Resilience Plan (NRRP), Mission 4, Component 2, Investment 1.1, Call for tender No. 1409 published on 14.9.2022 by the Italian Ministry of University and Research (MUR), funded by the European Union – NextGenerationEU – Project P2022KSTSR - Opto-mechanical effects in spin-defects for quantum technologies - CUP D53D23019370001, and PNRR MUR project PE_00000023 - SPOKE 4- CUP B53C22004170006. R.D.A, E.M. and D.G. from FBK acknowledge support from PNRR MUR project PE0000023-NQSTI- Spoke 4 and 8. The projects contributing to this work 20IND05 QADET and 23NRM04 NoQTeS have received funding from the European Partnership on Metrology, co-financed from the European Union's Horizon Europe Research and Innovation Programme and by the Participating States." The work by E.R. was supported by the MUR scholarship "PNRR DM 351/2022-M4C1".

Data Availability

The datasets used and/or analysed during the current study are available from the corresponding author on reasonable request.

Declarations

Competing interests

The authors declare no competing interests.

Author details

[1]University of Torino and Istituto Nazionale di Fisica Nucleare, sezione di Torino, 10125 Torino, Italy. [2]Istituto Nazionale di Ricerca Metrologica (INRiM), 10135 Torino, Italy. [3]Sensors & Devices Center, Fondazione Bruno Kessler, 38123 Trento, Italy. [4]Qnami AG, CH-4132 Muttenz, Switzerland.

Received: 10 December 2024 Accepted: 12 February 2025 Published online: 18 February 2025

References

1. Degen CL, Reinhard F, Cappellaro P. Quantum sensing. Rev Mod Phys. 2017;89(3):035002. https://doi.org/10.1103/RevModPhys.89.035002.
2. Gisin N, Thew R. Quantum communication. Nat Photonics. 2007;1(3):165–71. https://doi.org/10.1038/nphoton.2007.22.
3. Rondin L, Tetienne J-P, Hingant T, Roch J-F, Maletinsky P, Jacques V. Magnetometry with nitrogen-vacancy defects in diamond. Rep Prog Phys. 2014;77(5):056503. https://doi.org/10.1088/0034-4885/77/5/056503.
4. Chu Y, et al. Coherent optical transitions in implanted nitrogen vacancy centers. Nano Lett. 2014;14(4):1982–6. https://doi.org/10.1021/nl404836p.
5. Ruf M, Wan NH, Choi H, Englund D, Hanson R. Quantum networks based on color centers in diamond. J Appl Phys. 2021;130(7):070901. https://doi.org/10.1063/5.0056534.
6. Senkalla K, Genov G, Metsch MH, Siyushev P, Jelezko F. Germanium vacancy in diamond quantum memory exceeding 20 ms. Phys Rev Lett. 2024;132(2):026901. https://doi.org/10.1103/PhysRevLett.132.026901.
7. Bhaskar MK, et al. Quantum nonlinear optics with a germanium-vacancy color center in a nanoscale diamond waveguide. Phys Rev Lett. 2017;118(22):223603. https://doi.org/10.1103/PhysRevLett.118.223603.
8. Babinec TM, et al. A diamond nanowire single-photon source. Nat Nanotechnol. 2010;5(3):195–9. https://doi.org/10.1038/nnano.2010.6.
9. Mandel L, Wolf E. Optical coherence and quantum optics. Cambridge: Cambridge University Press; 1995. https://doi.org/10.1017/CBO9781139644105.
10. Deng X, et al. Quantum-enhanced metrology with large Fock states. Nat Phys. 2024. https://doi.org/10.1038/s41567-024-02619-5.
11. Zwinkels JC, Ikonen E, Fox NP, Ulm G, Rastello ML. Photometry, radiometry and 'the candela': evolution in the classical and quantum world. Metrologia. 2010;47(5):R15–32. https://doi.org/10.1088/0026-1394/47/5/R01.
12. Wang CS, et al. Efficient multiphoton sampling of molecular vibronic spectra on a superconducting bosonic processor. Phys Rev X. 2020;10(2):021060. https://doi.org/10.1103/PhysRevX.10.021060.
13. Brod DJ, et al. Photonic implementation of boson sampling: a review. Adv Photon. 2019;1(03):1. https://doi.org/10.1117/1.AP.1.3.034001.
14. Ourjoumtsev A, Ferreyrol F, Tualle-Brouri R, Grangier P. Preparation of non-local superpositions of quasi-classical light states. Nat Phys. 2009;5(3):189–92. https://doi.org/10.1038/nphys1199.
15. Jamieson DN, Lawrie WIL, Robson SG, Jakob AM, Johnson BC, McCallum JC. Deterministic doping. Mater Sci Semicond Process. 2017;62:23–30. https://doi.org/10.1016/j.mssp.2016.10.039.
16. Herzig T, Lühmann T, Räcke P, Scheuner C, Pezzagna S, Meijer J. Color center formation by deterministic single ion implantation. 2021. p. 1–30. https://doi.org/10.1016/bs.semsem.2020.09.001.
17. Wahl U, et al. Structural formation yield of GeV centers from implanted Ge in diamond. Mater Quantum Technol. 2024;4(2):025101. https://doi.org/10.1088/2633-4356/ad4b8d.
18. Pezzagna S, et al. Nanoscale engineering and optical addressing of single spins in diamond. Small. 2010;6(19):2117–21. https://doi.org/10.1002/smll.201000902.
19. Sangtawesin S, Brundage TO, Atkins ZJ, Petta JR. Highly tunable formation of nitrogen-vacancy centers via ion implantation. Appl Phys Lett. 2014;105(6):063107. https://doi.org/10.1063/1.4892971.
20. Vićentijević M, Jakšić M, Suligoj T. Implantation site design for large area diamond quantum device fabrication. Sci Rep. 2023;13(1):13483. https://doi.org/10.1038/s41598-023-40785-3.
21. Pacheco JL, et al. Ion implantation for deterministic single atom devices. Rev Sci Instrum. 2017;88(12):123301. https://doi.org/10.1063/1.5001520.
22. Wang J, et al. Scalable fabrication of single silicon vacancy defect arrays in silicon carbide using focused ion beam. ACS Photonics. 2017;4(5):1054–9. https://doi.org/10.1021/acsphotonics.7b00230.

23. Lesik M, et al. Maskless and targeted creation of arrays of colour centres in diamond using focused ion beam technology. Phys Status Solidi A. 2013;210(10):2055–9. https://doi.org/10.1002/pssa.201300102.
24. Tamura S, et al. Array of bright silicon-vacancy centers in diamond fabricated by low-energy focused ion beam implantation. Appl Phys Express. 2014;7(11):115201. https://doi.org/10.7567/APEX.7.115201.
25. Wan NH, et al. Large-scale integration of artificial atoms in hybrid photonic circuits. Nature. 2020;583(7815):226–31. https://doi.org/10.1038/s41586-020-2441-3.
26. Zhou Y, et al. Direct writing of single germanium vacancy center arrays in diamond. New J Phys. 2018;20(12):125004. https://doi.org/10.1088/1367-2630/aaf2ac.
27. Hollenbach M, et al. Wafer-scale nanofabrication of telecom single-photon emitters in silicon. Nat Commun. 2022;13(1):7683. https://doi.org/10.1038/s41467-022-35051-5.
28. Iwasaki T, et al. Germanium-vacancy single color centers in diamond. Sci Rep. 2015;5(1):12882. https://doi.org/10.1038/srep12882.
29. https://e6cvd.com/.
30. Radtke M, Render L, Nelz R, Neu E. Plasma treatments and photonic nanostructures for shallow nitrogen vacancy centers in diamond. Opt Mater Express. 2019;9(12):4716. https://doi.org/10.1364/OME.9.004716.
31. Nieto Hernandez E, et al. Efficient fabrication of high-density ensembles of color centers via ion implantation on a hot diamond substrate. Adv Phys Res. 2024. https://doi.org/10.1002/apxr.202400067.
32. Radtke M, Nelz R, Slablab A, Neu E. Reliable nanofabrication of single-crystal diamond photonic nanostructures for nanoscale sensing. Micromachines. 2019;10(11):718. https://doi.org/10.3390/mi10110718.
33. Momenzadeh SA, et al. Nanoengineered diamond waveguide as a robust bright platform for nanomagnetometry using shallow nitrogen vacancy centers. Nano Lett. 2015;15(1):165–9. https://doi.org/10.1021/nl503326t.
34. Brown KJ, Chartier E, Sweet EM, Hopper DA, Bassett LC. Cleaning diamond surfaces using boiling acid treatment in a standard laboratory chemical hood. J Chem Health Saf. 2019;26(6):40–4. https://doi.org/10.1016/j.jchas.2019.06.001.
35. Lachman L, Filip R. Criteria for single photon sources with variable nonclassicality threshold. New J Phys. 2019;21(8):083012. https://doi.org/10.1088/1367-2630/ab34b0.
36. Nieto Hernández E, et al. Efficiency optimization of Ge-V quantum emitters in single-crystal diamond upon ion implantation and HPHT annealing. Adv Quantum Technol. 2023;6(8):2300010. https://doi.org/10.1002/qute.202300010.
37. Doherty MW, Manson NB, Delaney P, Jelezko F, Wrachtrup J, Hollenberg LCL. The nitrogen-vacancy colour centre in diamond. Phys Rep. 2013;528(1):1–45. https://doi.org/10.1016/j.physrep.2013.02.001.
38. Fávaro de Oliveira F, Momenzadeh SA, Antonov D, Fedder H, Denisenko A, Wrachtrup J. On the efficiency of combined ion implantation for the creation of near-surface nitrogen-vacancy centers in diamond. Phys Status Solidi A. 2016;213(8):2044–50. https://doi.org/10.1002/pssa.201600326.
39. Pezzagna S, Naydenov B, Jelezko F, Wrachtrup J, Meijer J. Creation efficiency of nitrogen-vacancy centres in diamond. New J Phys. 2010;12(6):065017. https://doi.org/10.1088/1367-2630/12/6/065017.
40. Ziegler JF. Stopping of energetic light ions in elemental matter. J Appl Phys. 1999;85(3):1249–72. https://doi.org/10.1063/1.369844.
41. http://www.srim.org/.
42. Qadr HM, Hamad AM. Using of stopping and range of ions in matter code to study of radiation damage in materials. Radioelectron Nanosyst Inf Technol. 2020;12(4):451–6. https://doi.org/10.17725/rensit.2020.12.451.
43. Rauschenbach B. Ion Beam-Induced Damages. 2022. p. 71–122. https://doi.org/10.1007/978-3-030-97277-6_4.
44. Uzan-Saguy C, Cytermann C, Brener R, Richter V, Shaanan M, Kalish R. Damage threshold for ion-beam induced graphitization of diamond. Appl Phys Lett. 1995;67(9):1194–6. https://doi.org/10.1063/1.115004.
45. Fávaro de Oliveira F, et al. Tailoring spin defects in diamond by lattice charging. Nat Commun. 2017;8(1):15409. https://doi.org/10.1038/ncomms15409.
46. Grünwald P. Effective second-order correlation function and single-photon detection. New J Phys. 2019;21(9):093003. https://doi.org/10.1088/1367-2630/ab3ae0.
47. Kimble HJ, Dagenais M, Mandel L. Photon antibunching in resonance fluorescence. Phys Rev Lett. 1977;39(11):691–5. https://doi.org/10.1103/PhysRevLett.39.691.
48. Brouri R, Beveratos A, Poizat J-P, Grangier P. Photon antibunching in the fluorescence of individual color centers in diamond. Opt Lett. 2000;25(17):1294. https://doi.org/10.1364/OL.25.001294.
49. Corte E, et al. Magnesium-vacancy optical centers in diamond. 2022. arXiv:2206.08670.
50. Corte E, et al. Spectral emission dependence of tin-vacancy centers in diamond from thermal processing and chemical functionalization. Adv Photon Res. 2022;3(1):2100148. https://doi.org/10.1002/adpr.202100148.
51. Christinck J, et al. Bright single-photon emission from a GeV center in diamond under a microfabricated solid immersion lens at room temperature. J Appl Phys. 2023;133(19):193102. https://doi.org/10.1063/5.0150208.
52. Zifkin R, Rodríguez Rosenblueth CD, Janitz E, Fontana Y, Childress L. Lifetime reduction of single germanium-vacancy centers in diamond via a tunable open microcavity. PRX Quantum. 2024;5(3):030308. https://doi.org/10.1103/PRXQuantum.5.030308.
53. Nahra M, et al. Single germanium vacancy centers in nanodiamonds with bulk-like spectral stability. AVS Quantum Sci. 2021;3(1):012001. https://doi.org/10.1116/5.0035937.
54. Rogers LJ, et al. Electronic structure of the negatively charged silicon-vacancy center in diamond. Phys Rev B. 2014;89(23):235101. https://doi.org/10.1103/PhysRevB.89.235101.
55. Rugar AE, Dory C, Sun S, Vučković J. Characterization of Optical and Spin Properties of Single Tin-Vacancy Centers in Diamond Nanopillars. 2018. arXiv:1811.09941.
56. Schröder T, et al. Scalable focused ion beam creation of nearly lifetime-limited single quantum emitters in diamond nanostructures. Nat Commun. 2017;8(1):15376. https://doi.org/10.1038/ncomms15376.
57. Luo W, et al. Recent progress in quantum photonic chips for quantum communication and internet. Light: Sci Appl. 2023;12(1):175. https://doi.org/10.1038/s41377-023-01173-8.
58. Maring N, et al. A versatile single-photon-based quantum computing platform. Nat Photonics. 2024;18(6):603–9. https://doi.org/10.1038/s41566-024-01403-4.
59. Wang H, et al. Boson sampling with 20 input photons and a 60-mode interferometer in a 1014-dimensional Hilbert space. Phys Rev Lett. 2019;123(25):250503. https://doi.org/10.1103/PhysRevLett.123.250503.

Publisher's Note

Springer Nature remains neutral with regard to jurisdictional claims in published maps and institutional affiliations.

Submit your manuscript to a SpringerOpen journal and benefit from:

- ► Convenient online submission
- ► Rigorous peer review
- ► Open access: articles freely available online
- ► High visibility within the field
- ► Retaining the copyright to your article

Submit your next manuscript at ► springeropen.com